Journal of Environmental Chemical Engineering 14 (2026) 120529

Contents lists available at ScienceDirect

Journal of Environmental Chemical Engineering

journal homepage: www.elsevier.com/locate/jece

Removal of trace CH_4 emissions by warm O_2 plasma is kinetically limited: Insights from modeling and experiments

Matthias Albrechts [a,b,*,1], Stijn Helsloot [c,1], Ivan Tsonev [a,b], Niek den Harder [c], Gerard van Rooij [c], Annemie Bogaerts [a,b]

[a] Plasma lab for Applications in Sustainability and Medicine - ANTwerp (PLASMANT) and Center of Excellence PLASMA, Department of Chemistry, University of Antwerp, Groenenborgerlaan 171, Antwerp 2020, Belgium
[b] Electrification Institute, University of Antwerp, Olieweg 97, Antwerp 2020, Belgium
[c] Department of Circular Chemical Engineering, Faculty of Science and Engineering, Maastricht University, Maastricht 6229 EN, the Netherlands

ARTICLE INFO

Keywords:
Methane conversion
Microwave plasma
Chemical kinetics modeling
Rotational Raman spectroscopy

ABSTRACT

We investigate the potential of a warm O_2 plasma effluent for the removal of trace CH_4 concentrations in ambient air, using a combination of modeling and experiments. To parameterize the 0D model, rotational Raman measurements were performed to obtain both temperature and O atom concentration profiles downstream of the O_2 plasma. Subsequently, the model is validated by obtaining satisfactory agreement for CH_4 conversion and CO_2/CO/NO_x production with the experiments of [1]. Next, we explore the theoretical limits of the O_2 plasma effluent strategy by scanning the model over a broad range of effluent temperatures, mixing rates and ratios of plasma to barn air flow rate. Our model predicts the lowest energy cost for CH_4 conversion (at 100 ppm) to be 153 MJ/mol, obtained at a characteristic mixing time of 0.1 ms and flow rate ratio of 30 (plasma flow to barn air flow), which is still higher than that of catalytic thermal oxidation (ca. 120 MJ/mol). Based on these insights, we propose a new strategy that uses NO_x produced by warm air plasma to oxidize CH_4 at a catalyst surface, potentially reducing the required operating temperature and broadening the range of viable catalytic materials with higher resistance to poisoning than conventional Pd-based catalysts.

1. Introduction

Methane (CH_4) is a potent greenhouse gas with a global warming potential approximately 28 times greater than carbon dioxide (CO_2) over a 100-year period [2]. Its atmospheric concentration is predicted to increase to 2 ppm by the year 2030, a substantial rise from its preindustrial level of 0.7 ppm, correlating with a 0.5 °C increase above preindustrial temperatures [3]. An important strategy in reducing CH_4 emissions is the oxidation of CH_4 at its emission sources, where its concentration is higher than atmospheric levels [4].

For the control of point source CH_4 emissions, two main commercialized methods exist: regenerative thermal oxidation (RTO) [5], and catalytic thermal oxidation (CTO) [6]. Due to its high operating costs, the RTO method is suited for large air flows with CH_4 concentrations of 1000 ppm or higher, typically found in industrial settings [7]. However, Abernethy *et al.* [4] recently showed that around 3/4 of CH_4 emissions occur at concentrations below 1000 ppm.

CTO can treat lower CH_4 concentrations down to 200 ppm [8]. However, it faces other limitations, such as the size required to treat large air flows, rendering CTO methods inappropriate for agricultural and wastewater treatment applications, operating at scales exceeding 1 m^3 s^{-1} [7]. Additionally, highly active catalysts are required for the low-temperature combustion of the inert CH_4 molecule, such as Pd-based catalysts, which are susceptible to severe deactivation due to poisoning and sintering [6,9].

The pursuit of better alternatives for the oxidation of low CH_4 concentrations has led to the development of biofilters [10], photocatalysts [11], and catalysts combined with zeolites [12], but none have been proven at scale with an acceptable volumetric (kJ m^{-3}) or specific (kJ kg^{-1}) energy input [7,13]. We note that gas phase advanced oxidation (GPAO) is a promising strategy [14], in which reactive radical species are produced *in-situ* through the use of precursors photolyzed by UV

* Corresponding author at: Plasma lab for Applications in Sustainability and Medicine - ANTwerp (PLASMANT) and Center of Excellence PLASMA, Department of Chemistry, University of Antwerp, Groenenborgerlaan 171, Antwerp 2020, Belgium.
E-mail address: matthias.albrechts@uantwerpen.be (M. Albrechts).
[1] shared first author

https://doi.org/10.1016/j.jece.2025.120529
Received 18 September 2025; Received in revised form 7 November 2025; Accepted 29 November 2025
Available online 30 November 2025

lights. This method overcomes many limitations associated with catalysts, such as heat losses, high capital costs and deactivation of the catalyst. Recent work utilized chlorine atoms in gas phase that were created by photodissociation of Cl_2, reaching 58 % removal efficiency for a 50 ppm CH_4 flow at 30 slm, with relatively low energy cost of 2.1–7.7 kWh g^{-1} or 121–444 MJ/mol [7].

In the recent study of Helsloot *et al.* [1], a completely new strategy was explored that uses radicals present in a plasma effluent to activate the CH_4 molecules. Similar to gas phase radical generation in GPAO, this approach employs plasma to create reactive species, and subsequently, through the mixing of the plasma effluent with the low concentration CH_4 mixture, the radicals are titrated to the polluted air and CH_4 removal is initiated. In [1], the low-level CH_4 mixture was taken to be a barn air mixture, as livestock farming contributes approximately 14.5 % of total anthropogenic greenhouse gas emissions [15], but this strategy can be extended to other applications.

There exist various plasma types that could be explored for this application. Cold plasmas could have the advantage that no energy is lost in heating the gas mixture, but they are generally not energy-efficient for molecule dissociation, since a limited fraction of the electron energy is used in dissociative electron impact processes [16,17]. Additionally, cold plasma conditions often require low operating pressures, associated with high process costs [18,19]. Dielectric barrier discharge (DBD) plasma can operate at atmospheric pressure and maintain room temperature, but besides not being very energy-efficient, it encounters significant power losses associated with the high-frequency and high-voltage power supply [20]. Singh *et al.* [21] recently investigated oxidation of trace CH_4 concentrations (1 vol% in air) in a co-axial dielectric barrier discharge (DBD) quartz tube reactor, reaching a minimal energy cost of ca. 50 MJ per mole of converted CH_4. Since the energy cost of CH_4 conversion scales inversely proportional with CH_4 concentration, assuming CH_4 conversion is limitedly affected by the CH_4 level at such low concentrations [22], the energy cost is estimated to be two orders of magnitude higher for more realistic barn air concentrations of 100 ppm [1].

Warm or (quasi-)thermal plasmas, e.g., arc plasma and microwave (MW) plasma, are a more efficient source of radicals due to their high dissociation degrees linked to high plasma temperatures [23,24]. Therefore, Helsloot *et al.* [1] used a warm MW plasma, since it not only generates radicals efficiently, but can also operate with large gas flow rates and is free from impurities originating from electrode sputtering [25]. Hence, this MW plasma is further explored in the present study.

Due to the high energy costs associated with the elevated temperatures of warm MW plasma, the ratio of polluted air flow rate to plasma gas flow rate should be sufficiently high. Indeed, after mixing of both flows, the gas mixture should not heat up to temperatures around 1000 K, where the low CH_4 fraction would react spontaneously. Similar to RTO, the external heat needed to reach these temperatures is too high, since insufficient heat is generated from combustion of the low CH_4 fraction. Instead, the high radical fraction present in the plasma effluent should activate the CH_4 molecules upon mixing, enabling CH_4 conversion at relatively low temperatures (e.g. 450 °C), similar to those of CTO, or even lower.

Helsloot *et al.* [1] investigated various plasma-sustaining gases, and concluded that O_2 plasma was the only appropriate candidate, as it produced no hazardous or substantial by-products. While air plasma offers several practical advantages, including easier handling, lower cost, and reduced safety risks, the use of warm air plasma inevitably results in significant NO_x formation. In the O_2 plasma, reactive O atoms are created through O_2 dissociation, and they can oxidize CH_4 post-plasma via the reaction $O + CH_4 \rightarrow OH + CH_3$. However, injecting barn air close to the O_2 plasma at higher plasma powers can still lead to warm NO_x formation. A critical concern for the O_2 plasma effluent mixing is thus to mitigate NO_x formation and prevent substantial NO_x emissions, which could be harmful to the environment.

Helsloot *et al.* [1] achieved the best energy cost for CH_4 removal (EC_{CH_4}) by the O_2 plasma effluent at a flow rate ratio of 20 slm plasma flow to 19 slm barn air flow, resulting in 37.7 MJ/mol for a CH_4 concentration of 2400 ppm. This translates to an EC_{CH_4} of 905 MJ/mol for a more realistic barn air CH_4 concentration of 100 ppm, based on the assumption that the CH_4 conversion is independent of the injected CH_4 concentration at such low concentrations (this assumption will be evaluated later in this paper).

Catalytic thermal oxidation (CTO) via palladium catalysts is capable of converting low CH_4 concentrations within dry air at ca. 350 °C [26]. However, in practical CH_4 abatement scenarios, impurities such as water vapor are commonly present in the gas stream. It was shown in [27] that the presence of H_2O significantly diminishes the activity of Pd/Al_2O_3 catalysts at lower temperatures, necessitating operating conditions around 450 °C to achieve efficient CH_4 oxidation. Similar findings were reported in [28], where low-temperature deactivation of Pd/Al_2O_3 due to water vapor required comparable temperatures for near-complete CH_4 conversion. Given that realistic barn air compositions contain substantial H_2O fractions ($>$ 1000 ppm) [29], we adopt 450 °C as the benchmark operating temperature for CTO. At this temperature, the associated energy cost for CH_4 conversion, assuming a CH_4 concentration of 100 ppm, is ca. 120 MJ/mol. When compared to the energy cost of post-plasma O atom-activated CH_4 conversion reported in [1], CTO is about 7.5 times more energy efficient.

These results indicate that it will be challenging for post-plasma O atom activated CH_4 conversion to reach the EC_{CH_4} of thermal catalysis. However, Helsloot *et al.* [1] also demonstrated that EC_{CH_4} can be significantly reduced by increasing the barn air flow rate relative to the plasma flow rate. Nevertheless, due to the reactor configuration employed in [1], specifically, tangential barn air injection downstream of the plasma, the maximum achievable flow rate ratio of barn air flow to plasma flow was limited to 1. Higher injection rates resulted in substantial backflow of barn air into the plasma zone, leading to plasma instability and eventual extinguishment. However, improved reactor designs, incorporating reactor constrictions downstream of the plasma, would likely allow for higher flow rate ratios of barn air flow to plasma flow, since backflow of the barn air to the plasma zone can be eliminated through injection of the barn air after the constriction. In addition, turbulence generated after the gas expansion would increase the mixing rate, as is typical for nozzle expansion chambers [30], further improving the CH_4 activation.

Before investigating these advanced experimental setups, we use the model presented in this paper to explore whether higher flow rate ratios of barn air to plasma flow and higher plasma energy inputs, as well as higher mixing rates, i.e., conditions that could not be explored in the experiments by Helsloot *et al.* [1] due to plasma stability issues, might reduce the energy cost, potentially bringing it below that of CTO.

To explore the theoretical limits of this plasma effluent strategy, we have developed a 0D chemical kinetics model. This model describes the post-plasma gas conversion process occurring when the effluent of warm O_2 plasma mixes with the barn air. We first validate the model by reproducing the experimental measurements from [1]. To strengthen the model validation, rotational Raman measurements were performed to obtain both temperature and O atom concentration profiles downstream of the O_2 plasma. Subsequently, we investigate the influence of the plasma effluent temperature, flow rate ratio and mixing rate, with the aim of maximizing the CH_4 conversion and minimizing the energy cost and NO_x production.

2. Experimental details

The reactor previously used to measure the CH_4 conversion was modified by adding a laser to the original setup [1]. The new setup thus consists of five main parts, as illustrated in Fig. 1.

A solid-state microwave power generator (2450 MHz, $<$1 kW) is used for plasma generation. The microwave generator is isolated via a circulator so that reflected microwaves are absorbed by a water load. An

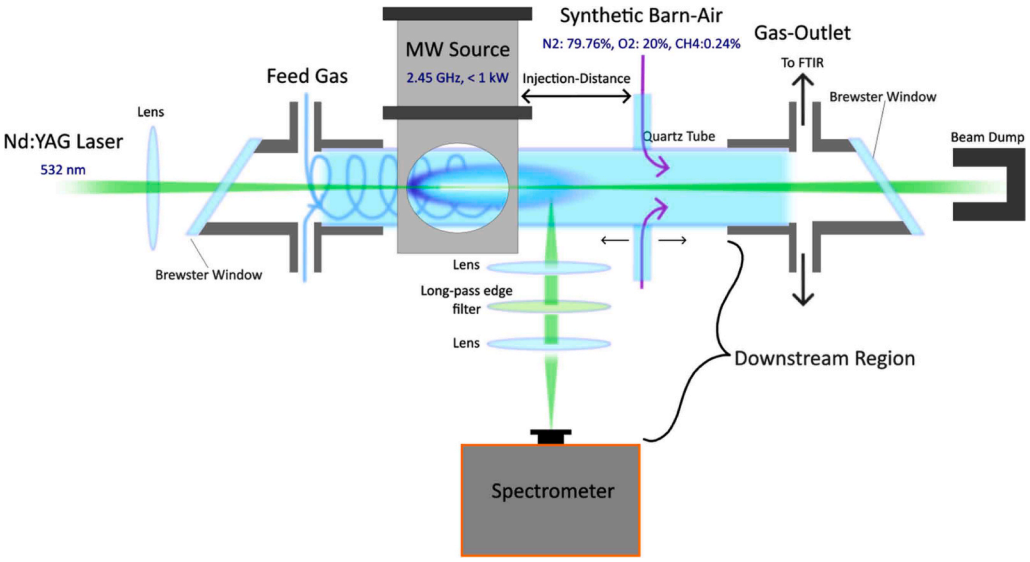

Fig. 1. Schematic illustration of the reactor setup. The injection-distance is adjustable in steps of 2 cm, ranging from 2 to 14 cm. The feed gas (O_2) is injected into a vortex configuration. Two Nd:YAG lasers are combined and are shot through the setup as a single laser beam.

autotuner ensures minimal reflected power by matching the impedance of the circuit. The microwave power absorbed by the plasma is corrected for the reflected power.

The plasma is sustained in a quartz tube with 26 mm inner diameter and 420 mm length. A secondary gas inlet with an inner diameter of 1 mm is positioned at different distances along the tube, ranging from 150 to 270 mm in steps of 20 mm. The flow rates of the plasma-sustaining gas and downstream-injected gas are regulated by mass flow controllers (MFCs), expressed in standard liters per minute (SLM). The synthetic barn air is created by mixing 2400 ppm of CH_4 into air (~80 % N_2, 20 % O_2), which is injected downstream of the O_2 plasma. As most of our previous work was done for a ratio of O_2 to synthetic barn air of 4, this same ratio is used in the present work.

The reactor output gas flows through a 20.062 cm path length gas cell with germanium (Ge) windows. The pressure in the gas cell is kept low (100 mbar) to minimize pressure broadening of the experimental spectra. Measurements are conducted using an Invenio R FTIR spectrometer. The Invenio R uses a Michelson interferometer combined with a liquid-nitrogen-cooled mercury cadmium telluride photovoltaic detector. The effluent concentrations are calculated by fitting data from the HITRAN database to the experimental data [31].

The rotational Raman setup uses two 532 nm Nd:YAG lasers (Litron ltd.) which are combined before passing through the full length of our reactor. Two lasers are combined to improve the signal-to-noise ratio, which is especially needed at high temperatures. With this laser diagnostic, we aim to measure spontaneous rotational Raman scattering, which is inelastic scattering with a change in rotational quantum number. Since this effect is relatively weak, the elastic (Rayleigh scattering) is removed from our final spectra by using a 532 nm RazorEdge long-pass filter (LP03–532RE-25). The measurements are performed using an Andor iStar spectrometer. Due to the sudden increase in transmission of the filter, the measured spectral lines below 534.9 nm are ignored (Raman shift of 100 cm^{-1}). Both lasers and the spectrometer are all phase-matched using a pulse delay generator. The reactor is positioned on a translational stage, allowing us to make 2D maps of the temperature and O atom concentration directly downstream of our plasma region and inside of the mixing region. Both temperature and O atom concentration are plotted as a function of power, radial and axial downstream distance. The measurable radial distance goes from 0 to 8 mm in steps of 2. The axial downstream distance is defined as the distance between the waveguide and our measurement point, which is at 15, 30, 40, 50, 70 and 100 mm.

Our measured spectra are fitted using an in-house created method to calculate the expected Raman spectra [32], based upon many previous works looking into spontaneous Raman spectroscopy [33–37]. This method allows us to assess the local gas composition and temperature downstream of the plasma, without having to calibrate for the system's collection efficiency. Also, as the wavelength region of the measured spectra is narrow and we cut off any overlap with the edge of the notch filter, wavelength calibration is not necessary. In this method, the local gas composition is not determined in absolute values, but only in relative terms. This is only correct if all components present in the gas mixture are effectively measured and accounted for. Further explanation, as well as an example spectrum, are given in the supplementary information (section S.2).

3. Model description

To explore the theoretical limits of post-plasma O atom activated CH_4 conversion, we have developed a 0D chemical kinetics model in the framework of the Chemical Reaction Engineering module of COMSOL Multiphysics [38]. The construction of this model closely follows the methodology outlined in [39]. Here, we briefly discuss the most important features and direct the reader to [39] for a more detailed discussion.

The model solves the 0D mass balance equations for a batch reactor, given by:

$$\frac{d(c_i V)}{dt} = R_i V \tag{1}$$

where c_i is the species molar concentration, V denotes the simulation volume and R_i is the species rate expression resulting from chemical reactions. We adopt the GRI-Mech 3.0 reaction set [40], which is an optimized mechanism designed to model CH_4 combustion in air, containing 53 different species and 325 different reactions. Surface recombination of O atoms is not included in our model, as it is expected to be negligible under the current reactor conditions [23], specifically, an internal diameter of 13 mm and operation at atmospheric pressure, leading to much faster gas-phase recombination than diffusion of O atoms to the reactor walls. The reactor volume is adjusted to keep a constant pressure, balancing variations in temperature and number density:

$$\frac{dV}{dt} = \frac{V}{T}\frac{dT}{dt} + \frac{RT}{p}V\sum_i R_i \tag{2}$$

with R the ideal gas constant, T the gas temperature and p the pressure in the reactor (1 atm).

Fig. 2 schematically illustrates the experimental setup as implemented in our global mixing model. The upper section depicts the reactor tube transporting the hot O_2 plasma effluent, with barn air injected downstream through tangential inlets. The lower section illustrates the conceptual framework of the global model, beginning at the initial volume V_0 and extending to the final simulation volume V_f.

We approximate the O_2 plasma effluent as a combination of a hot gas stream that has passed through the plasma and a surrounding cold stream at 300 K that has not. Indeed, MW plasma at atmospheric pressure is typically "contracted", with a hot plasma core surrounded by a colder periphery, so not all the gas passes through the hot plasma core [41–43]. Immediately after the plasma, the hot gas stream represents the plasma stream generated by the contracted MW plasma. However, as the gas travels downstream, the cold surrounding gas mixes with the inner hot gas core, which increases the cross-section of the hot gas stream, while decreasing its temperature, in addition to the cooling caused by conductive losses to the walls. Consequently, the radius and temperature of the hot gas stream are a function of the distance from the plasma outlet, and barn air injected at different positions downstream will encounter varying O/O_2 mixtures.

We model this by adjusting the radius (R_T) and temperature (T_i) of the hot gas stream, ensuring that the heat required to heat up the cold O_2 to the hot dissociated mixture does not exceed the experimental energy input:

$$SEI_p = \frac{P}{F_p} > \frac{R_T^2}{R^2}\left[n_{eq} * H_{O_2,eq}(T_i) - H_{O_2}(T_{cold})\right] \tag{3}$$

where SEI_p is the plasma specific energy input, P is the experimental power, F_p is the plasma molar flow rate (mol/s), R is the reactor tube radius, $T_{cold} = 300$ K, H_{O_2} (J/mol) is the enthalpy of O_2, $H_{O_2,eq}$ (J/mol) is the enthalpy of the dissociated oxygen equilibrium mixture and n_{eq} is a factor that accounts for the increase in number of particles of the dissociated chemical equilibrium mixture. The ratio $\frac{R_T^2}{R^2}$ corresponds to the ratio of the hot O_2/O gas stream to the total O_2 plasma flow, as can be deduced from Eq. 4 below. In addition to this first requirement, we account for the heat lost through the reactor walls, by ensuring that the total mixture enthalpy (kJ/mol), i.e., the right-hand side of Eq. 3, decreases along the reactor length.

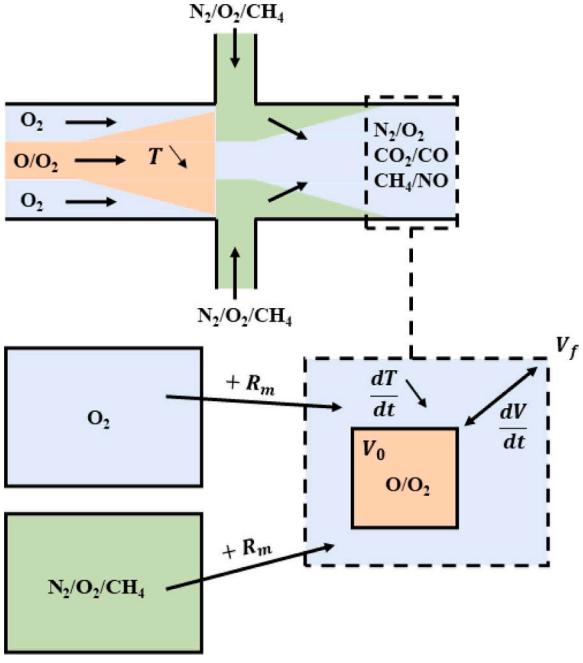

Fig. 2. Schematic of the experimental setup (upper part) and conceptual framework of the global model (lower part).

The initial composition within the simulation represents the hot gas stream, at the position of barn air injection. Since we showed in [39] that the O_2 plasma afterglow contains an equilibrium fraction of O atoms at atmospheric pressure, the initial O_2/O densities are determined from the dissociation equilibrium at the temperature of the hot gas stream. The presence of O atoms at their equilibrium fraction in the plasma effluent is further supported by the Raman measurements presented in the current study, as discussed in Section 4.

When barn air is injected post-plasma, N_2 (80 %), O_2 (20 %) and CH_4 (400 – 2400 ppm) mix with the hot (plasma) gas stream (O_2/O) and the cold surrounding O_2 stream. We model this mixing of gases by adding $N_2/O_2/CH_4$ (300 K) to the simulation volume, as illustrated in Fig. 2, where the cold O_2 added includes both the cold surrounding stream and the O_2 present in the barn air. Thus, we consider diffusive mass transfer from the surrounding cold O_2 stream and the injected barn air to the inner hot gas stream, but we neglect diffusion from the latter to the surrounding stream. Indeed, we assume that conversion does not occur in the cold surrounding stream due to slow reaction kinetics. In this way, we can describe the system in a single kinetic simulation.

The molar ratios of the cold surrounding O_2 stream to the hot O_2/O gas stream, and of the injected barn air flow to the hot O_2/O gas stream are determined by the molar flow rates and the radius of the hot gas stream (R_T):

$$\frac{n_{cold}}{n_{hot}} = \frac{R^2 - R_T^2}{R_T^2} \tag{4}$$

$$\frac{n_{air}}{n_{hot}} = \frac{R^2}{R_T^2} * \frac{F_{air}}{F_p} \tag{5}$$

where n_{hot}, n_{cold} and n_{air} represent the molar amounts of hot O_2/O mixture, cold O_2 gas and barn air in the simulation, respectively, and F_p (mol/s) and F_{air} (mol/s) are the molar flow rates of O_2 plasma and barn air, respectively.

We introduce a mixing rate R_m (mol/s) that determines the rate at which the gases mix in the reactor, i.e. how fast $N_2/O_2/CH_4$ (300 K) are added to the simulation. Therefore, the mixing rate is a source term (R_m/V_r) in the species rate expression (cf. R_i in Eq. 1), representing the diffusive mass transfer from the surrounding stream to the simulation volume. The mixing rate R_m is defined by an exponential decay, as explained in [39].

$$R_m = -\frac{d(n(t))}{dt} = \frac{n_{tot}}{\tau_{mix}} e^{-t/\tau_{mix}} \tag{6}$$

where n_{tot} is the total amount of gas (mol) that is added, and τ_{mix} is the characteristic mixing time.

The temperature of the gas mixture is calculated in the heat-balance equation [39]:

$$\rho C_p \frac{dT}{dt} = -\frac{R_m^{N_2/O_2/CH_4}}{V_r}\left(H_{N_2/O_2/CH_4}(T) - H_{N_2/O_2/CH_4}(T_{cold})\right) - \frac{k(T - T_{wall})}{R^2} + Q_R \tag{7}$$

where ρ is the gas density, C_p denotes the heat capacity, H is the species enthalpy, k is the thermal conductivity of the mixture, $T_{wall} = 300$ K and Q_R is the total heat absorbed/released in chemical reactions. The first term on the right-hand side represents the cooling of the mixture due to mixing with the cold $N_2/O_2/CH_4$ gas, accounting for the energy needed to heat up the incoming gas to the current temperature T in the simulation volume. We note that $R_m^{O_2}$ represents the addition of cold O_2, including both the cold surrounding stream as well as the

O_2 present in the cold barn air.

The CH_4 conversion (χ^{CH_4}) is calculated as:

$$\chi^{CH_4} = \frac{x_{CH_4} n_{air} - [CH_4]_f V_f}{x_{CH_4} n_{air}} \quad (8)$$

where x_{CH_4} is the molar fraction of CH_4 present in the barn air (ppm), and $[CH_4]_f$ and V_f are the final molar concentration present in the simulation and the final reactor volume, respectively.

We note that, compared to the 0D framework adopted in this work, higher-dimensional models can more accurately capture the mixing dynamics between barn air and plasma flow through species diffusion at the flow interfaces. Unfortunately, multidimensional models, describing the highly complex and turbulent flow field, characterized by swirling flow, steep gradients in temperature, velocity, and mixture composition near the plasma interface, as well as tangential flow injection, in combination with the extensive reaction chemistry involved in CH_4 oxidation in air (e.g., the GRIMECH 3.0 mechanism includes 53 species and 325 reactions), would be extremely challenging to develop and also computationally highly demanding. Consequently, we first explore the reaction chemistry using a 0D model in this work. This approach allows us to efficiently scan a broad operational parameter space and assess the feasibility of the proposed strategy.

4. Experimental Results

Our first aim is to map both temperature and gas composition (i.e., O atom concentration) downstream of the O_2 plasma, without synthetic barn air injection downstream. The following measurements were done with an O_2 feed flow rate of 20 slm and a pressure of 1 atmosphere (1020 mbar). The results are displayed in Fig. 3.

From Fig. 3 (left), we learn that the O_2 plasma is efficient in transporting heat downstream. We can quantify this by integrating the temperature profiles radially. In the 400 W case, considering the 8 mm cylinder in which the measurements were done, we find that approximately 75 % of the initial (thermal) energy at 15 mm is still present at 100 mm (assuming constant pressure). Notably, an increase in power has a positive effect on both the maximum temperature as well as the transport of heat to the downstream, as in all other cases, approximately 85 % of the initial (thermal) energy at 15 mm is still present at 100 mm.

Heat loss to the surroundings is often complex and influenced by many factors, but it is rarely inversely dependent on temperature gradients (i.e. the heat loss becoming smaller with higher temperatures) [44]. Thus, we hypothesize that the observed increase in "transport-efficiency" for higher powers is due to the measurements being performed over a radius of 8 mm compared to the full reactor radius of 13 mm.

In Fig. 3 (right), we note that the O atom concentration follows a similar pattern as the temperature, as the O atoms travel further downstream for higher powers. We may compare these results with the maps obtained when synthetic barn air is injected downstream at a downstream distance of 40 mm, as shown in Fig. 4. The O_2 feed flow rate is kept at 20 slm, with a downstream injection flow rate of 5 slm. The pressure is kept at 1 atmosphere (1020 mbar).

In Fig. 4, during downstream injection of synthetic barn air, the O atom concentration (right) still closely follows the measured temperature profile (left). After the downstream injection point (40 mm), we see a drastic decrease in temperature. The same decrease can be seen for the O atom concentration, with barely any O atoms being present further downstream. Note that at 400 and 500 W, the temperature is mostly uniform at 100 mm, showing relatively fast mixing. At 600 and 700 W, we can see that the core remains hotter than the outer regions, demonstrating that the feed and downstream injected flow are not completely mixed yet.

An assumption for the proposed model is that without mixing, the O/O_2 ratio follows thermal chemical equilibrium at atmospheric pressure [23]. Combining the results from Fig. 3 (left and right), this assumption can be verified, as shown in Fig. 5. When no downstream injection of synthetic barn air is present, the O/O_2 ratio closely follows the values predicted by thermal chemical equilibrium, validating this initial assumption.

When injecting synthetic barn air downstream, we aim to create a region where the O/O_2 ratio is decoupled from temperature, i.e., where an elevated O atom fraction can be sustained that allows energy-efficient removal of the low CH_4 fraction, as will be explained in Section 6. Combining the results from Fig. 4 (left and right), we plot the O/O_2 ratio as a function of temperature whilst injecting synthetic barn air downstream, as also shown in Fig. 5.

It is important to realize that due to dilution with N_2 downstream, the O/O_2 ratio predicted by thermal chemical equilibrium may differ slightly, as shown in Fig. 5. Here, we take 25 % as an example, as this is

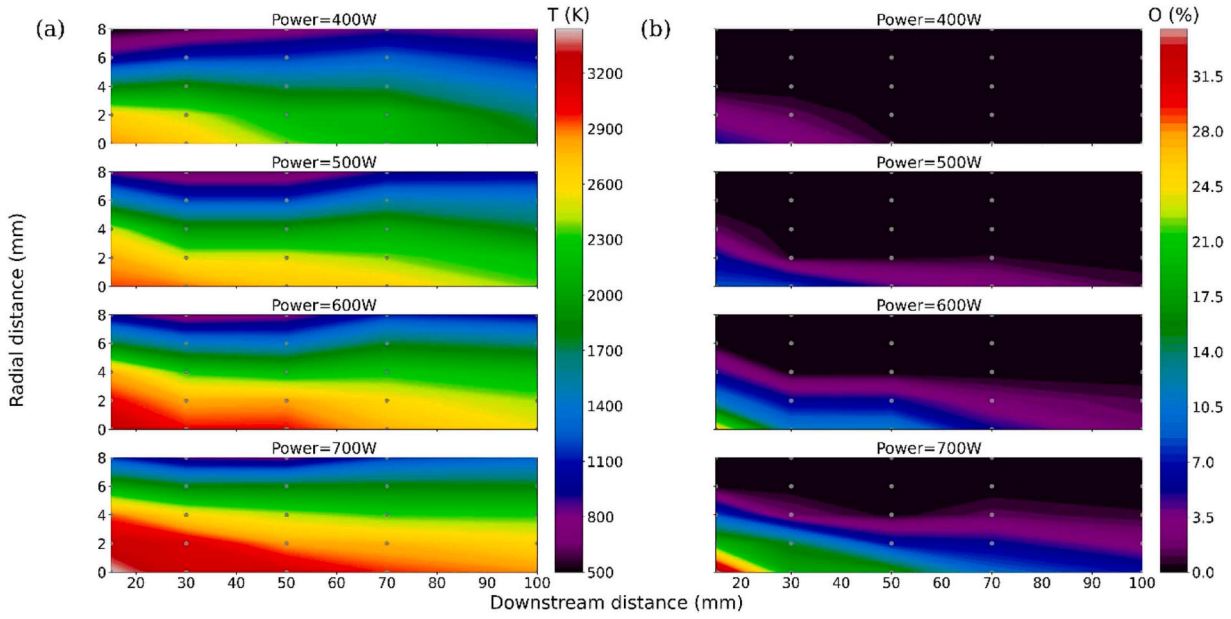

Fig. 3. Measured temperature (left) and O atom concentration (right) in the downstream region of an O_2 plasma, as a function of axial and radial distance for different microwave powers. The measurement points are given as grey dots.

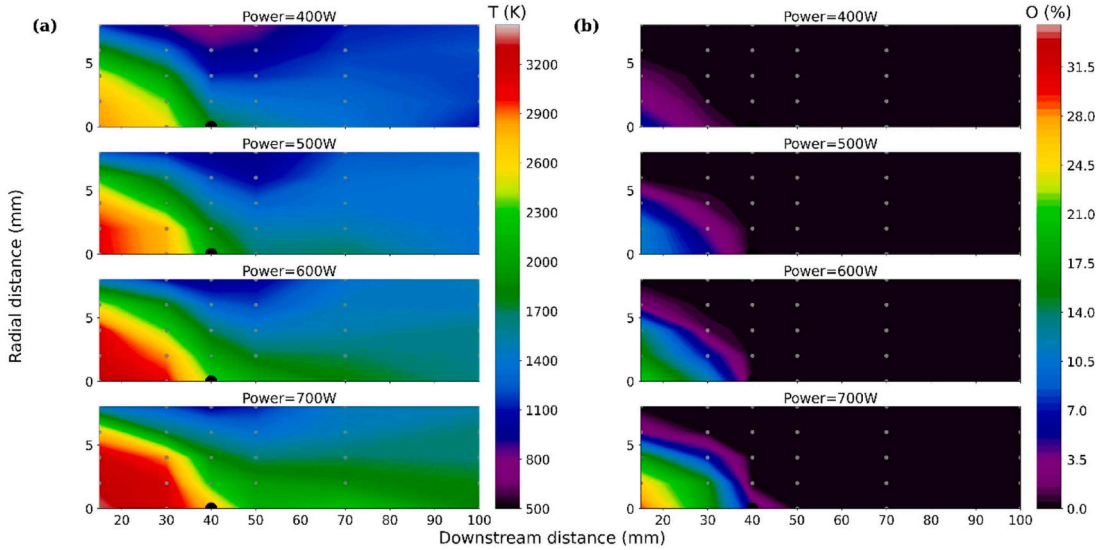

Fig. 4. Measured temperature (left) and O atom concentration profiles (right) in the downstream region of an O_2 plasma with synthetic barn air injected at a downstream distance of 40 mm. The measurement points are given as grey dots, with the point of injection given as a black dot.

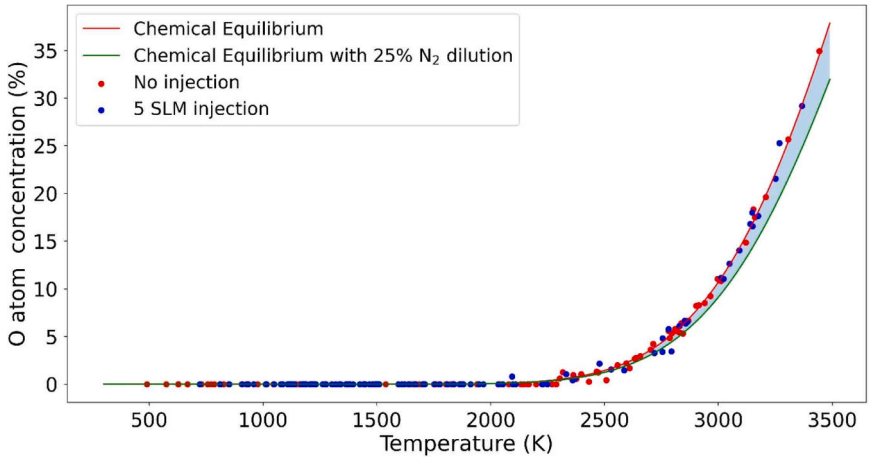

Fig. 5. Measured (symbols) O atom concentrations as a function of temperature, as well as calculated values based on thermal chemical equilibrium (solid lines, with and without dilution with N_2).

the highest measured dilution. However, this change is small for lower temperatures, and higher temperature regions match with lower dilution. Because of this, we believe it valid to assume the O/O_2 ratio once again closely follows the predicted values by thermal chemical equilibrium. These results indicate that within these measurements, O atom recombination is sufficiently fast so that the O atom fraction immediately relaxes towards its equilibrium value upon mixing and cooling of the gas mixture. Consequently, higher flow rate ratios of barn air flow to plasma flow and higher mixing rates are needed to perform better than thermal conversion, as will be discussed in Section 6.

5. Model Validation

To assess the ability of our model to accurately simulate the post-plasma conversion process, we applied it to the experimental setup involving the mixing of O_2 plasma effluent with synthetic barn air, as described in [1]. In these experiments, the plasma power, the inlet position of barn air injection relative to the plasma outlet, and the barn air flow rate were systematically varied (power = 400 – 700 W, inlet position = 2 – 14 cm, and barn air flow rate = 5 – 20 slm) to evaluate their impact on CH_4 conversion and NO production. Therefore, the concentrations of CH_4, CO_2, CO, and NO were measured at the outlet, and their trends are extensively discussed in [1]. The concentrations are plotted without their respective uncertainties, because in all cases, the uncertainties are below 5 ppm and are not clearly visible within the graphs. Further information on how the fitting procedure works for FTIR data can be found on Github [31].

5.1. Specification of model parameters

Based on the temperature measurements of the downstream plasma region conducted in the present study, we adjusted the model parameters to correctly describe the experiment. These parameters include the radius and temperature of the hot gas core, R_T and T_i in Eq. 3, respectively, and the characteristic mixing time τ_{mix} (cf. Eq. 6). As an initial guess, we selected for T_i the measured on-axis temperature of the O_2 plasma flow without post-plasma $N_2/O_2/CH_4$ injection (Fig. 3, left) at the point of CH_4 injection. Subsequently, we varied R_T and T_i to optimize the agreement for CH_4 conversion and $CO_2/CO/NO_x$ concentrations between the model calculations and experimental data, ensuring that the chosen values did not significantly deviate from the experimental profiles by visual inspection.

The optimized values for R_T and T_i are shown in Table 1, as well as the total mixture enthalpy. We note that the values for T_i are somewhat lower than the experimental on-axis temperature (cf. Fig. 3, left), while the R_T values are somewhat higher than the experimental width of the hot gas zone (cf. Fig. 3, left). These discrepancies are attributed to the limitations of our global model, which represents the hot gas zone using a uniform mixture temperature. Nevertheless, we believe this represents reasonable agreement, given the approximative nature of the 0D model.

The experimental temperature profiles also serve as a validation tool for the mixing rate employed in the model. Upon the injection of barn air, the temperature in the simulation predominantly cools due to mixing with the cold gas. Therefore, the cooling rate predicted by the model, governed by the selected value for τ_{mix}, should be of a similar magnitude to that observed in the experiments.

Since the experiment operates under steady-state conditions, the temperature at a fixed spatial location remains constant over time. Consequently, the cooling experienced by the gas along the flow path is governed solely by the convective term of the total derivative [45]. To quantify the experimental cooling rate from the spatial temperature profiles, we correlate the distance traveled by the gas downstream to specific points in time using the gas flow velocity, solving the following differential equation:

$$\frac{dx}{dt} = \frac{F_0}{A} * \frac{\rho(T(x))}{\rho_0} \tag{9}$$

Here, x is the axial position in the reactor, A is the reactor tube diameter, F_0 and ρ_0 denote the volumetric flow rate and mass density of oxygen gas at 300 K, respectively, and $\rho(T)$ is the mass density of the equilibrium oxygen mixture at the specified temperature, taken as the on-axis temperature at the given axial position x.

By solving the differential equation described above, the axial temperature can be mapped as a function of time, providing a rough estimate of the cooling rate experienced by the gas downstream. When solving Eq. 9 for the temperature profile corresponding to a plasma power of 700 W and a post-plasma CH_4 injection distance of 4 cm (Fig. 4, left), we estimate a cooling rate of $1 - 2 \times 10^5$ K/s during the first 7 ms. Assuming a characteristic mixing time of 10 ms, the cooling rate in the model decreases from 5×10^5 K/s at the start of the simulation to 5×10^4 K/s at t = 7 ms. Therefore, as $\tau_{mix} = 10$ ms produces cooling rates comparable to the experimental estimate and achieves reasonable agreement with the experimental data, we have adopted this value for all conditions for the sake of simplicity.

5.2. Comparison between model calculations and experiments

Fig. 6 shows the CH_4 conversion (left y-axis), as well as the formed CO_2, CO and NO_x ($NO + NO_2$) concentrations (right y-axis) as a function of barn air injection position (relative to the plasma outlet), comparing the model calculations and experiments for plasma powers of 500 W (a) and 700 W (b), and plasma and barn air flow rates of 20 slm and 5 slm, respectively. Under certain conditions (inlet position of 2 – 6 cm for P = 500 W and inlet position of 10 – 14 cm for P = 700 W) the CO concentration is somewhat underestimated and the CO_2 concentration somewhat overestimated, which indicates over-oxidation of CO to CO_2. Nevertheless, in general reasonable agreement is reached, and we believe our model sufficiently captures the observed trends, considering the simplicity of the 0D framework.

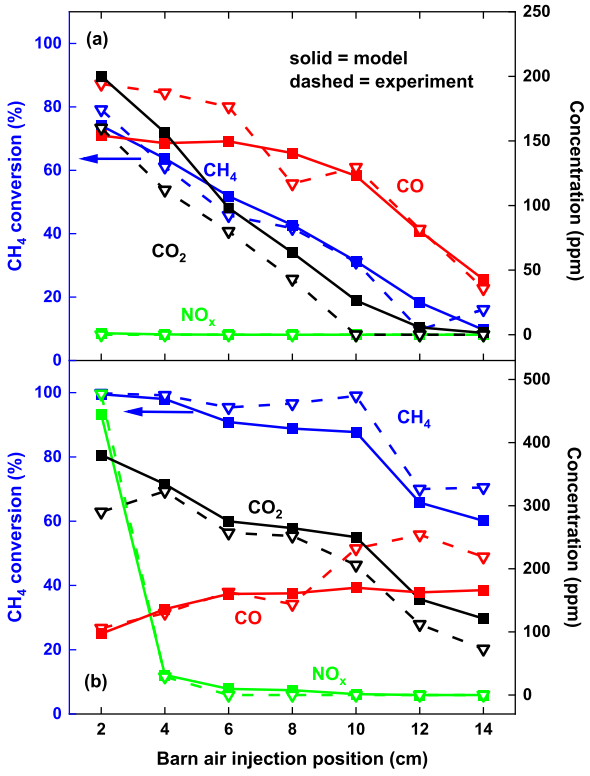

Fig. 6. Conversion of CH_4 (left y-axis) in blue and formed CO_2, CO, and NO_x concentrations (right y-axis) in black, red and green, respectively, as a function of inlet position of barn air injection, for a power of 500 W (a) and 700 W (b), and plasma and barn air flow rates of 20 slm and 5 slm, respectively. Modeling results are indicated by solid lines, experimental measurements by dashed lines. The experimental uncertainties are always below 5 ppm and thus not visible.

Overall, at P = 500 W, the CH_4 conversion, and the produced CO and CO_2 concentrations drop upon later injection positions, which makes sense, as the O/O_2 plasma effluent cools down as a function of position due to wall heat losses and, consequently, the O atom concentration decreases as the gas travels downstream. The CH_4 conversion drops more or less linearly from almost 80 % to about 15 % upon increasing the injection position from 2 to 14 cm, while the formed CO and CO_2 concentrations drop from 150 to 200 ppm to below 50 ppm, and virtually no NO_x seems to be formed at P = 500 W. At P = 700 W, the CH_4 conversion is nearly 100 % for injection positions up to 10 cm, and only drops to 60–70 % for the injection position of 14 cm. The formed CO_2 concentration drops from ca. 300 to ca. 100 ppm upon increasing injection position, while the CO concentration rises from ca 100 to ca. 200 pm, pointing towards over-oxidation of CO to CO_2 at the shortest injection positions. Strikingly, at P = 700 W, almost 500 ppm of NO_x is formed at the injection position of 2 cm, but it drops to negligible values for injection positions of 4 cm and above. Thus, it is clear that at P = 700 W and short injection positions, there are abundant O radicals to make the CH_4 conversion quite effective, but due to the high gas temperatures enabling N_2 oxidation, there is also significant NO_x formation. All these trends are comprehensively discussed in [1], so to avoid redundancy, we refer the reader to [1] for a detailed explanation.

In addition to varying the barn air injection position, we also investigated the effect of increasing barn air flow rate relative to plasma flow rate. Fig. 7 presents a comparison between the model predictions

Table 1
Model parameter values for R_T and T_i used to describe the experiments with varying $N_2/O_2/CH_4$ injection position at a plasma power of 500 and 700 W. Additionally, the total mixture enthalpy H_{mix} is given in the last column.

	P = 500 W			P = 700 W		
Inlet position (cm)	T_i (K)	R_T (mm)	H_{mix} (kJ/mol)	T_i (K)	R_T (mm)	H_{mix} (kJ/mol)
2	2343	7.8	26.6	2950	7.2	36.9
4	2213	7.8	24.5	2627	7.8	32.4
6	1976	8.0	22.1	2521	7.8	30.0
8	1838	8.0	20.1	2499	7.8	29.5
10	1629	8.2	18.0	2339	8.2	29.4
12	1544	8.2	16.8	2100	8.2	25.2
14	1501	8.2	16.1	1967	8.4	24.2

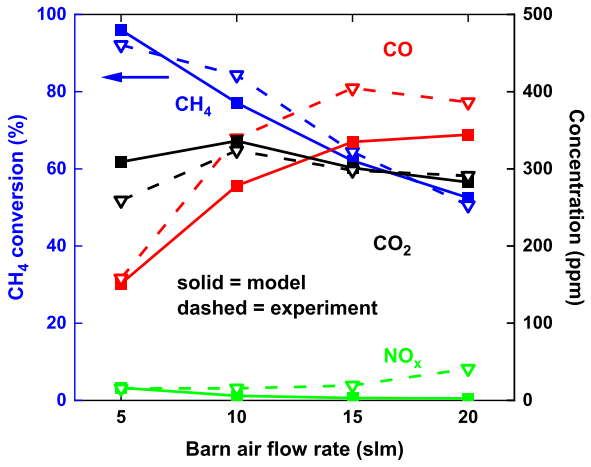

Fig. 7. Conversion of CH_4 (left y-axis) in blue and formed CO_2, CO, and NO_x concentrations (right y-axis) in black, red and green, respectively, as a function of barn air flow rate, for a power of 620 W, plasma flow rate of 20 slm and barn air injection position of 4 cm after the plasma outlet. Modeling results are indicated by solid lines, experimental measurements by dashed lines. The experimental uncertainties are always below 5 ppm and thus not visible.

and experimental data [1] for CH_4 conversion (left y-axis) and formed CO_2, CO, and NO_x concentrations (right y-axis), as a function of the barn air injection flow rate, for a fixed plasma flow rate of 20 slm, power of 620 W and barn air injection position of 4 cm after the plasma outlet. Since the barn air injection position remains constant, we assume a constant radius and temperature of the inner hot gas stream at the point of barn air injection. We obtain reasonable agreement between model and experiment for $R_T = 7.9$ mm and $T_i = 2550$ K, values which are close to the parameters used to describe the experiment at the plasma power of 700 W and injection distance of 4 cm ($R_T = 7.8$ mm and $T_i = 2627$). The CH_4 conversion drops from almost 100 % to ca. 50 % upon increasing the barn air flow rate from 5 to 20 slm. It is logical that higher conversions are reached at lower barn air fractions compared to plasma flow. The produced CO concentration, however, rises from ca. 140 to almost 400 ppm, while the CO_2 concentration stays relatively constant around 300 ppm, and the NO_x concentration stays also very low for all barn air flow rates.

In Fig. 6, where we modelled the experiments with varying barn air injection position, we considered a constant characteristic mixing time of $\tau_{mix} = 10$ ms. In contrast, for the present case, the characteristic mixing time is reduced as the barn air flow rate increases, since we believe higher injection rates will improve the penetration of the barn air to the O_2 flow, significantly increasing the contact surface between both and therefore enhancing diffusion and mass transfer. This higher mixing rate upon increasing barn air flow rate allows better agreement with experiment. Consequently, we reduce the characteristic mixing time from $\tau_{mix} = 10$ ms for the barn air flow rate of 5 slm to $\tau_{mix} = 3.33$ ms and $\tau_{mix} = 2$ ms for barn air flow rates of 10 slm, and 15 and 20 slm, respectively. While the model again somewhat overestimates the oxidation of CO to CO_2, we believe it captures the experimental trends sufficiently well.

By capturing the trends in CH_4 conversion, as well as CO_2, CO, and NO_x production, while adhering to the physical constraints derived from experimental measurements, such as reasonable temperatures and mixing rates, we believe our model sufficiently captures the post-plasma chemistry and gas flow mixing. This enables us to make qualitative assertions and explore the theoretical limits of the strategy beyond the experimentally investigated parameter range, as discussed in the next section.

6. Theoretical limits of post-plasma O atom activated CH_4 conversion

After validating our model, we investigate the best energy cost (EC) achievable for O atom activated CH_4 conversion through mixing of an O/O_2 plasma effluent with low concentrations of CH_4 in a barn air mixture. As mentioned in the Introduction, Helsloot *et al.* [1] obtained the best EC_{CH_4} of 37.7 MJ/mol for a CH_4 concentration of 2400 ppm (equivalent to 905 MJ/mol for a more realistic barn air CH_4 concentration of 100 ppm) at a flow rate ratio of 20 slm plasma flow to 19 slm barn air flow. This is 7.5 times higher than the EC_{CH_4} associated with catalytic thermal oxidation (CTO), i.e., 120 MJ/mol. However, higher flow rate ratios of barn air flow to plasma flow, associated with higher mixing rates (as discussed in previous section), that were not explored in the experiments of [1], might still significantly reduce the EC_{CH_4}. Therefore, in this section, we aim to identify the optimal plasma effluent temperature, flow rate ratio, and mixing rate that minimize EC_{CH_4}, while also minimizing NO_x production to prevent harmful NO_x emissions. In particular, we aim to evaluate whether the current strategy can become competitive with existing CH_4 removal methods like CTO.

To investigate the theoretical limits of post-plasma O atom activated CH_4 conversion, our focus here is not on simulating a specific experimental setup. Instead, we conduct more conceptual simulations. For simplicity, we assume that all the O_2 passes through the plasma and neglect conductive losses to the walls. These conditions resemble the scenario of barn air injection at the end of a homogeneous warm O_2 plasma. Consequently, the molar ratio of the hot dissociated oxygen mixture (O_2/O) to barn air is determined by the flow rate ratio of both:

$$\frac{n_{air}}{n_{O_2}} = \frac{F_{air}}{F_{O_2}} \tag{10}$$

where n_{air} and n_{O_2} represent the molar amounts of barn air and hot O_2/O mixture, respectively, and F_{air} (mol/s) and F_{O_2} (mol/s) are the molar flow rates of barn air and O_2 plasma, respectively.

6.1. *Effect of mixing rate on CH_4 conversion, NO_x production and energy cost*

We first focus on the effect of the mixing rate, determined by the characteristic mixing time τ_{mix} (cf. Eq. 6). Fig. 8 presents the modeling results as a function of O_2 plasma effluent temperature, for τ_{mix} values of 1 ms, 0.1 ms and 0.01 ms, and for a barn air / plasma flow rate ratio of 8 and a barn air CH_4 concentration (x_{CH_4}) of 100 ppm. The CH_4 conversion, NO_x concentration and EC_{CH_4} are plotted in Fig. 8(a), (b) and (c), respectively. The energy cost per mole of CH_4 is calculated as the energy required to heat up and dissociate the cold O_2 gas to the hot O_2/O equilibrium mixture at the plasma effluent temperature, divided by the number of moles of converted CH_4:

$$EC_{CH_4} = \frac{\left[n_{eq} * H_{O_2,eq}(T_i) - H_{O_2}(T_{cold})\right] * F_{O_2}}{x_{CH_4} F_{air} * \chi^{CH_4}} \tag{11}$$

We note that this represents the ideal limit, as energy will be lost through wall losses in the plasma, and the plasma afterglow will cool down before it mixes with the barn air at the injection point.

As shown in Fig. 8(a), CH_4 conversion increases with the afterglow temperature, attributed to the higher density of O atoms in the effluent and enhanced reaction kinetics. Additionally, Fig. 8(a) illustrates how the mixing rate (i.e., the inverse of mixing time) impacts CH_4 conversion: higher conversions are achieved with faster mixing rates, provided the afterglow temperature is sufficiently high. Conversely, at lower afterglow temperatures, higher mixing rates result in lower conversions. This phenomenon can be attributed to two competing effects.

First, faster mixing (i.e., shorter mixing time) corresponds to faster cooling (cf. Eq. 7). Consequently, for a given number of moles of barn air introduced into the system, more O atoms will be available because they

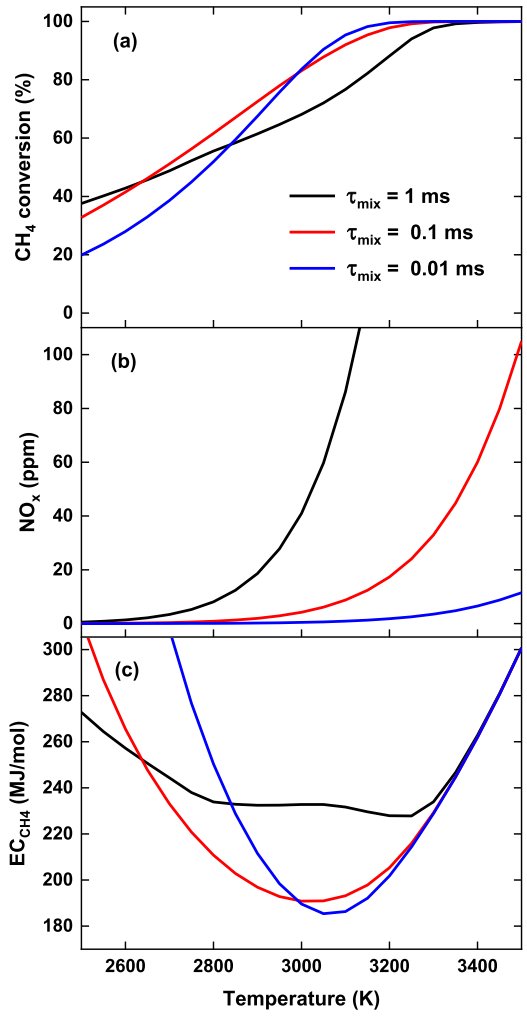

Fig. 8. CH_4 conversion (a), formed NO_x concentration (b) and energy cost of CH_4 conversion (c) as a function of O_2 plasma effluent temperature for different mixing rates (or mixing times), with $x_{CH_4} = 100$ ppm, for a flow rate ratio of barn air flow to plasma flow of 8.

have had less time to recombine. This kinetic drag for O atom recombination is illustrated in Fig. 9, where the O atom fraction (left y-axis) is plotted as a function of the total amount of barn air added to the

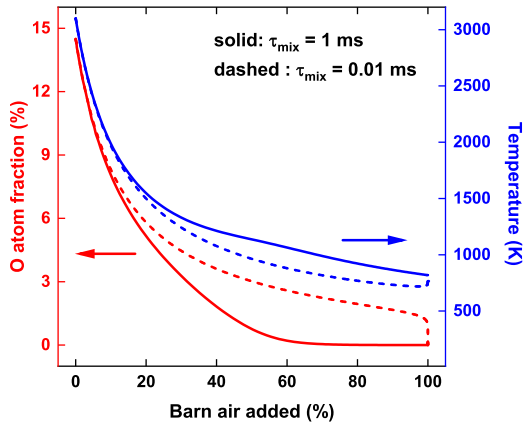

Fig. 9. O atom fraction (left y-axis) and mixture temperature (right y-axis) as a function of the total amount of barn air added to the system, for a characteristic mixing time of 1 ms (solid) and 0.01 ms (dashed), for $T_i = 3100$ K and flow rate ratio of barn air flow to plasma flow of 8.

simulation. We note that due to limited O atom recombination, the O atom fraction is much higher than its equilibrium fraction. For instance, equilibrium calculations within the Cantera Python module [46] for air with a 100 ppm CH_4 concentration at the temperature of 1000 K yield an O atom equilibrium fraction of only 7.7×10^{-11}, which is much lower than the O atom fractions of approximately 1 % and ca. 3 % obtained at the mixture temperature of around 1000 K at $\tau_{mix} = 1$ ms and $\tau_{mix} = 0.01$ ms, respectively.

The elevated O atom fraction observed in the simulations (cf. Fig. 9) was not detected in the experiments (cf. Fig. 5). The reason is that the cooling rate considered in these conceptual calculations is considerably higher than that estimated for the experiment (cf. Section 5), i.e., the initial cooling rate in the simulation of 2×107 K/s at the lowest mixing rate (corresponding to $\tau_{mix} = 1$ ms) is two orders of magnitude higher than the cooling rate of 2×105 K/s estimated for the experiment. The higher cooling rate is attributed to both the shorter mixing time of $\tau_{mix} = 1$ ms in the model compared to $\tau_{mix} = 10$ ms estimated for the experimental conditions, and the higher flow rate ratio of plasma flow to barn air flow of 8 in the model compared to 1/4 in the experiment. As a result of the higher cooling rate, O atoms have insufficient time to recombine and reach their equilibrium concentration, leading to the elevated O atom fraction observed in the simulations.

We note that below temperatures of ca. 2000 K in the experiments, the O atom fraction plotted in Fig. 5 might exceed its equilibrium value due to the slower reaction kinetics. However, this deviation cannot be reliably quantified owing to the limited sensitivity of the measurement technique (ca. 0.5 %). The higher presence of O atoms for a given amount of barn air added at higher mixing rates allows for more interaction with CH_4 molecules, thereby increasing the rate of CH_4 oxidation and enhancing CH_4 conversion, at sufficiently high temperature. In addition, the temperature is plotted on the right y-axis of Fig. 9, indicating that during the mixing process the temperature is slightly lower for $\tau_{mix} = 0.01$ ms, as less heat has been generated through the exothermic O atom recombination process.

Besides the higher presence of O atoms at higher mixing rates, which enhances conversion, a second crucial factor is that O atoms react more effectively with CH_4 at elevated temperatures, while at lower temperatures O atom recombination will become more important, because it has a lower or negligible enthalpic barrier. As a result, the rate of CH_4 activation by O atoms strongly decreases with respect to the rate of O atom recombination at lower temperatures. In this way, fast cooling reduces CH_4 conversion as the O atoms react, on average, at a lower temperature. At lower afterglow temperatures, this second effect dominates and faster mixing decreases the overall conversion, as seen in Fig. 8(a). Conversely, at higher afterglow temperatures, the first effect becomes more important, and a higher mixing rate improves the CH_4 conversion.

Fig. 8(b) indicates that the NO_x concentration increases with rising temperature, as O atoms more effectively react with inert N_2 at higher temperatures. Notably, Fig. 8(b) also shows that the NO_x production is strongly reduced upon increasing mixing rate, since faster cooling limits the timeframe for thermal NO_x formation. It is clear that the characteristic mixing time should be preferably below 1 ms, since at $\tau_{mix} = 1$ ms, a high NO_x concentration of 173 ppm is obtained at the effluent temperature of 3200 K, corresponding to $\chi^{CH_4} = 86$ %.

Finally, Fig. 8(c) illustrates that the energy cost per mole of CH_4 decreases with increasing temperature, as the improved conversion outweighs the higher energy input. Only at high conversion (>90 %), the energy cost rises with increasing temperature because the higher energy input is no longer offset by the additional conversion of the small fraction of remaining CH_4. In addition, lower energy costs can be achieved for higher mixing rates, which are associated with higher conversions. The best energy cost for the flow rate ratio of 8 is achieved at $T_i = 3100$ K and $\tau_{mix} = 0.01$ ms, yielding $EC_{CH_4} = 192$ MJ/mol. While this value is much better than the EC_{CH_4} of 905 MJ/mol, extrapolated for CH_4

concentrations of 100 ppm from the experiments in [1], unfortunately, it is still significantly higher than the target EC_{CH_4} of 120 MJ/mol of CTO.

We observe that EC_{CH_4} can be significantly reduced when decreasing τ_{mix} from 1 ms to 0.1 ms, i.e., from 228 kJ/mol to 191 kJ/mol. However, further reduction of τ_{mix} yields diminishing returns, with $\tau_{mix} = 0.01$ ms resulting in $EC_{CH_4} = 185$ MJ/mol. Increasing the mixing rate beyond this point will even increase the energy cost. The reason is that for $\tau_{mix} < 0.01$ ms, the O atom fraction reaches its upper limit as the timescale for O atom recombination becomes longer than the timescale for O atom addition through gas mixing. Consequently, the drop in the O atom fraction observed in Fig. 9 for $\tau_{mix} = 0.01$ ms is mainly due to dilution. Hence, at these high mixing rates, only the effect of slower CH_4 activation by O atoms at lower temperatures (see discussion above) contributes, and increasing the mixing rate lowers the conversion, thereby increasing EC_{CH_4}.

6.2. Effect of flow rate ratio on CH_4 conversion, NO_x production and energy cost

While the energy cost EC_{CH_4} cannot be further lowered by increasing the mixing rate, it can still be reduced by increasing the flow rate ratio of barn air to plasma flow. Hence, we now evaluate the impact of the flow rate ratio on the CH_4 conversion, NO_x production and energy cost. Similar to Fig. 8 discussed above, Fig. 10 plots the CH_4 conversion, NO_x concentration and EC_{CH_4} in (a), (b) and (c), respectively, for different flow rate ratios of barn air flow to plasma flow, as a function of the O_2 plasma effluent temperature, with $\tau_{mix} = 0.1$ ms and $x_{CH_4} = 100$ ppm. Fig. 10 (a) indicates that higher effluent temperatures are needed to reach a similar CH_4 conversion at higher flow rate ratio. Trivially, the mixture cools down more as more cold barn air is added, which increases O atom recombination and reduces the O atom fraction available for CH_4 oxidation. This makes it harder to convert all the CH_4 present, thus necessitating higher effluent temperatures.

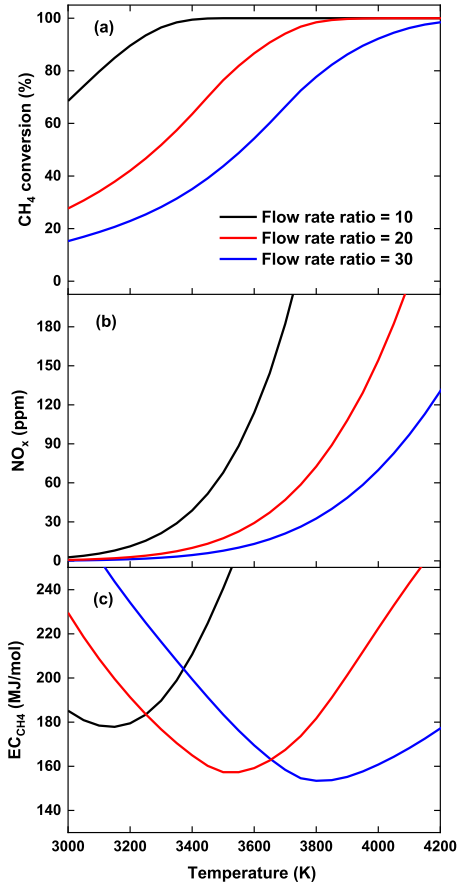

Fig. 10. CH_4 conversion (a), NO_x concentration (b) and energy cost of CH_4 conversion (c) as function of O_2 plasma effluent temperature for different flow rate ratios, with $\tau_{mix} = 0.1$ ms and $x_{CH_4} = 100$ ppm.

Fig. 10 (b) indicates that for a given effluent temperature the NO_x concentration decreases with increasing flow rate ratio of barn air flow to plasma flow, as higher barn air flow rates lead to stronger cooling. However, considering that higher effluent temperatures are needed to reach the same conversion at higher flow rate ratios (Fig. 10 (a)), in order to reach the same conversion the NO_x concentration is actually higher for higher flow rate ratios, e.g., for $\chi^{CH_4} = 93$ %, the flow rate ratio of 10 yields a NO_x concentration of 16 ppm at $T_i = 3250$ K, while the flow rate ratio of 30 yields a NO_x concentration of 72 ppm at $T_i = 4000$ K.

Fig. 10 (c) indicates that the energy cost of CH_4 conversion (EC_{CH_4}) can be significantly reduced by increasing the flow rate ratio of barn air flow to plasma flow, considering that higher effluent temperatures are needed, e.g., the minimal EC_{CH_4} of 178 MJ/mol at $T_i = 3150$ K and $\chi^{CH_4} = 85$ % for the flow rate ratio of 10 can be reduced to $EC_{CH_4} = 153$ MJ/mol at $T_i = 3850$ K and $\chi^{CH_4} = 85$ % for the flow rate ratio of 30. The drop in EC_{CH_4} at higher flow rate ratios of barn air to plasma flow, combined with higher effluent temperatures, is caused by multiple effects.

Before we discuss these effects, we first consider the case where barn air is heated to a temperature of ca. 1000 K, causing the low CH_4 fraction (e.g., 100 ppm) to react spontaneously, which we will refer to as thermal conversion. In this context, the removal of CH_4 is initiated by the reaction $O + CH_4 \rightleftharpoons OH + CH_3$, of which the forward net rate is two orders of magnitude higher than the thermal dissociation of CH_4 (i.e., $CH_4 + M \rightleftharpoons CH_3 + H + M$) in our kinetic simulation for a CH_4 concentration of 100 ppm and temperature of 950 K. Subsequent reactions with the generated CH_x and H radicals further contribute to CH_4 conversion. This means that at the temperature where thermal conversion occurs, the equilibrium fraction of O atoms is sufficiently high to initiate the removal of the low CH_4 fraction.

We now consider the case where the kinetics of O atom recombination are infinitely fast. This implies that when the hot mixture cools down due to mixing with the cold barn air, the O atom density immediately relaxes towards its equilibrium fraction. Consequently, the conversion of CH_4 will cease at temperatures below approximately 1000 K, as from that point onward, insufficient O atoms are present to convert the low CH_4 fraction in the newly added barn air, similar to the case of thermal conversion.

Note that in the case of infinitely fast O atom recombination, there is no point in starting from a hot O_2/O mixture with a high O atom fraction and mixing it with cold barn air. Indeed, it will produce the same result as simply heating the barn air to the temperature reached when the hot O_2/O mixture fully mixes with the barn air. Here, we disregard the fact that the increased O_2 fraction from adding the O_2 plasma effluent would require a slightly lower mixture temperature for CH_4 removal, as this leads to a negligible reduction in energy cost. In this case of infinitely fast O atom recombination, the energy cost associated with post-plasma CH_4 conversion would be even higher than thermal conversion since all the heat needed to raise the temperature of the additional O_2 to the final temperature is lost. We note that this scenario corresponds to the experimental conditions of [1], where, as demonstrated in Section 5 (cf. Fig. 5), O atoms rapidly relax to their equilibrium fraction upon mixing with barn air, owing to the relatively slow mixing rate characteristic of the experimental setup.

When the barn air flow rate is increased relative to the plasma flow rate, the discharge gas (O_2) constitutes a smaller fraction of the total effluent. Consequently, a smaller fraction of the energy input is lost as heat captured by the discharge gas at the effluent temperature. This effect primarily explains the strong drop in EC_{CH_4} observed in [1] when

the flow rate ratio of barn air to plasma flow is increased, e.g., for F_{O_2} = 20 slm, a power of 620 W, and a CH_4 concentration of 2400 ppm (as used in the experiments of [1], instead of the more realistic value of 100 ppm for barn air considered in this work), EC_{CH_4} = 83 MJ/mol at F_{air} = 5 slm and EC_{CH_4} = 37.7 MJ/mol at F_{air} = 19 slm.

However, O atom recombination kinetics are not infinitely fast, and higher mixing rates can result in an elevated O atom fraction for a given amount of barn air added, as was illustrated in Fig. 9. In addition to the fact that a smaller fraction of the energy input is lost as heat captured by the discharge gas at higher flow rate ratios of barn air to plasma flow, higher flow rate ratios also lead to higher absolute mixing and cooling rates, thus improving conversion and energy cost as well. This is similar to the lower EC_{CH_4} achieved at higher mixing rates associated with lower characteristic mixing times, as explained in Section 6.1.

In addition to the higher absolute cooling rate, the higher initial effluent temperature suited for higher flow rate ratios is also advantageous. Indeed, the O atom fraction increases significantly as the equilibrium fraction of O atoms sharply rises with temperature, e.g. at T = 3150 K and T = 3850 K, x_O^{eq} = 17 % and x_O^{eq} = 65 %, respectively. As a result, the kinetic drag can more effectively sustain an elevated O atom fraction during the mixing process, thereby improving conversion.

We observe that EC_{CH_4} can be significantly reduced when increasing the flow rate ratio of barn air flow to plasma flow from 10 to 20, i.e., from 178 kJ/mol to 157 kJ/mol (Fig. 10 (c)). However, further reduction of the flow rate ratio to 30 leads to progressively smaller improvements, achieving a minimal energy cost of EC_{CH_4} = 153 MJ/mol. Indeed, the energy gained by reducing the discharge gas fraction becomes increasingly smaller. In addition, the absolute cooling rate associated with τ_{mix} = 0.1 ms for the flow rate ratio of 8 was already near its optimal value (cf. Fig. 10 (c)), so increasing the absolute mixing rate by increasing the flow rate ratio at τ_{mix} = 0.1 ms yields diminishing returns. Consequently, increasing the flow rate ratio above 30 does not reduce EC_{CH_4} further, but will only increase NO_x production, as discussed above.

Because of the kinetic drag on O atom recombination, an elevated O atom fraction will be maintained at temperatures below 1000 K, enabling the conversion of the low CH_4 fraction at temperatures lower than those required for thermal conversion. Consequently, the optimal energy cost of EC_{CH_4} = 153 MJ/mol achieved with the current post-plasma O atom activated CH_4 conversion strategy is significantly lower than the energy required to heat air to the temperature at which the low CH_4 concentration reacts spontaneously. For example, a 100 ppm CH_4 concentration completely reacts within 1 s at 1020 K, associated with an energy cost of 224 MJ/mol.

However, the best EC_{CH_4} of 153 MJ/mol is still quite high, and considerably higher than that of thermal catalysis (120 MJ/mol). The primary reason for the high energy cost is the rapid rate of O atom recombination compared to the rate of CH_4 activation by O atoms. We note that our kinetic analysis indicates that O atom recombination does not only occur via the direct channel of three-body recombination, but in larger extent proceeds through a circular reaction mechanism involving an H atom, illustrated in Fig. 11. Because of the high recombination rate, proceeding via different channels, even when an elevated O atom fraction can be sustained at high mixing rates, nearly all O atoms will eventually recombine into O_2 instead of reacting with CH_4 molecules. Consequently, the high energy cost associated with dissociating the O_2 discharge gas is predominantly lost to O atom recombination, resulting in the relatively high lower limit of EC_{CH_4} = 153 MJ/mol for post-plasma O atom activated CH_4 conversion. We note that this is the theoretical lower limit predicted by our model, but in reality, EC_{CH_4} is likely significantly higher due to heat losses within the plasma reactor associated with the high plasma temperatures [47].

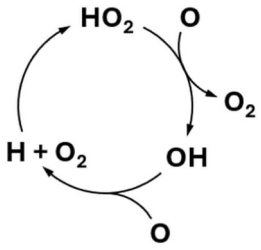

Fig. 11. Reaction mechanism of H atom assisted O atom recombination.

Besides the high energy cost, achieving the high flow rate ratios of barn air flow to plasma flow (> 20) and high mixing rates (τ_{mix} < 0.1 ms), necessary to obtain the optimal energy cost and minimize NO_x production, is likely very challenging from an experimental perspective. This is indicated by the highest flow rate ratio of barn air flow to plasma flow of 1 achieved in [1], attributed to plasma stability problems. As discussed in the introduction, higher flow rate ratios may be attainable by implementing secondary injection of barn air downstream of a constriction, thereby reducing backflow of cold air into the plasma zone. However, it remains uncertain whether ratios as high as 20 or more can be achieved using this approach.

Although uncommon, sub-millisecond mixing timescales can be achieved in highly specialized reactor configurations. For example, microreactors with small characteristic length scales [48,49] can achieve mixing times on the order of 0.1 ms, though their low throughput likely renders them unsuitable for CH_4 abatement applications requiring treatment of large exhaust volumes. In supersonic combustion systems, fuel must mix with air within tens of microseconds to enable efficient combustion, suggesting that similarly fast mixing may be achievable using advanced setups involving supersonic nozzles or shock generators [50,51]. However, such configurations would incur additional energy costs and could pose substantial challenges for scale-up.

Given these limitations, the realistic energy cost for the current strategy is likely to exceed the lower bound of EC_{CH_4} = 153 MJ/mol predicted by our modeling at a flow rate ratio of 30 and τ_{mix} = 0.1 ms. Quantitative estimation remains difficult due to uncertainties in the achievable conditions within more specialized and optimized reactor designs. Considering the significantly lower energy cost of thermal catalysis (ca. 120 MJ/mol), we conclude that post-plasma O atom activated CH_4 conversion is unlikely to be a viable alternative to existing CH_4 removal technologies.

6.3. *Effect of CH_4 concentration on CH_4 conversion, NO_x production and energy cost*

Lastly, we examine the effect of the CH_4 concentration (x_{CH_4}) on the CH_4 conversion (χ^{CH_4}), NO_x production and energy cost. Fig. 12 plots

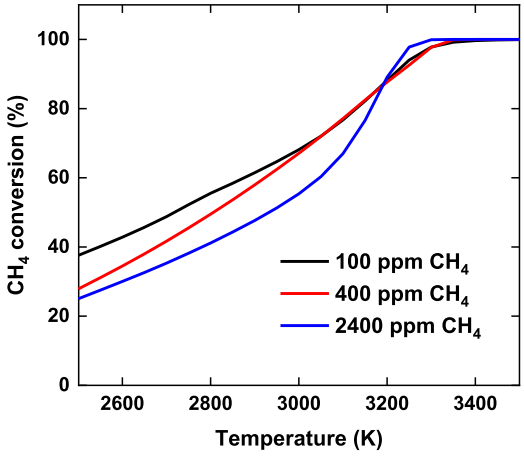

Fig. 12. Conversion of CH_4 for different CH_4 concentrations, as a function of the effluent temperature, for a flow rate ratio of barn air to plasma flow of 8 and τ_{mix} = 0.1 ms.

χ^{CH_4} as a function of the effluent temperature. Clearly, the conversion depends on the CH_4 concentration, with the largest relative difference seen at the lowest temperature of 2500 K, i.e., $\chi^{CH_4} = 37.5$ % and $\chi^{CH_4} = 25$ % for $x_{CH_4} = 100$ ppm and $x_{CH_4} = 2400$ ppm, respectively. However, the 1.5-fold difference in conversion is much smaller than the 24-fold difference in concentration, suggesting that the conversion is relatively insensitive to the CH_4 concentration.

The reason is that the fraction of O atoms consumed in CH_4 activation is very small compared to O atom recombination. Consequently, the O atom fraction is primarily determined by the mixture temperature and reaction time, governed by the flow rate ratio and mixing rate, as extensively discussed in Sections 6.1 and 6.2. However, converting higher concentrations of CH_4 requires more time for a given O atom fraction, which is why the conversion is somewhat lower for higher concentrations. At elevated temperatures, the reaction kinetics accelerate, and the relative difference becomes very small for $T > 3150$ K, associated with CH_4 conversions of around 85 %. Therefore, when looking at high conversion degrees that are favourable for the energy cost, we believe it is a reasonable assumption to state that for the current strategy, the CH_4 conversion is independent of the injected CH_4 concentration at the low concentrations considered here. Consequently, EC_{CH_4} will vary inversely proportional to the CH_4 concentration, e.g., for $T = 3000$ K, EC_{CH_4} is equal to 191, 59 and 12 MJ/mol for a CH_4 concentration of 100, 400 and 2400 ppm, respectively.

Finally, the NO_x production is also relatively insensitive to CH_4 concentration, e.g., for $T = 3500$ K, the NO_x concentration is equal to 105, 106 and 111 ppm for a CH_4 concentration of 100, 400 and 2400 ppm, respectively. This can again be attributed to the minimal influence of CH_4 concentration on the mixture temperature and O atom concentration, which are the primary factors governing NO_x formation, as discussed earlier.

7. Perspective

As mentioned above, because of the high energy cost (minimum 153 MJ/mol for $x_{CH_4} = 100$ ppm) of the current strategy and the challenging experimental conditions needed, we believe post-plasma O atom activated CH_4 is not a more viable alternative to existing trace CH_4 removal methods, such as catalytic thermal oxidation. The high energy cost is attributed to the rapid rate of O atom recombination at atmospheric conditions, shown in the experimental results, relative to the rate of CH_4 activation. However, the concept of plasma technology to generate reactive species for efficient removal of low CH_4 fractions might still hold value.

In the case of post-plasma O atom chemistry, the introduction of a catalyst could enable reaction pathways that enhance oxidation of CH_4 over O atom recombination. Still, rapid gas-phase recombination limits the time available for O atoms to reach the catalyst surface. For instance, for the flow rate ratio of 8 and $\tau_{mix} = 0.01$ ms, the flow is quenched within the 0.01 ms timescale, but due to the kinetic drag, the O atom fraction will drop below 10 ppm after ca. 1 ms. Below this concentration, CH_4 conversion stops as insufficient O atoms are present to activate the CH_4 molecules. Therefore, from the point where complete mixing is achieved within 0.01 ms, the O atoms must reach the catalyst surface within 1 ms. For a diffusion constant of 1.5×10^{-4} m^2/s, this corresponds to a diffusion length of 0.4 mm, indicating the challenging reactor setup needed to meet these requirements.

Li *et al.* [52] investigated atmospheric pressure plasma jet (APP-J)-assisted CH_4 oxidation over a Ni-SiO_2/Al_2O_3 catalyst, demonstrating a strong correlation between the quantified fluxes of plasma-produced O atoms and CH_4 oxidation at the catalyst surface. This correlation indicates that, within their experimental setup, O atoms are able to reach the catalyst surface and actively participate in CH_4 oxidation. Notably, the study employed low O_2 concentrations (<1.5 %) in the Ar/O_2 plasma jet, which slows down O atom recombination due to the involvement of O_2 in the recombination mechanism (cf. Fig. 11), thereby extending the lifetime of the O atoms. Furthermore, since O atoms are convectively transported into the catalytic bed, a sufficiently high volumetric flow rate is required to ensure effective delivery. However, the low total gas throughput (<0.6 slm) used in [52] may present challenges for scaling the process to practical CH_4 abatement applications.

Given the limited potential of O atoms as oxidants for CH_4 due to their short lifetimes, it could be interesting to investigate other reactive species produced by plasma for CH_4 oxidation that are more stable, such as ozone (O_3) and nitrogen oxides (NO_x). The addition of NO_x to the barn air offers several advantages over conventional catalytic thermal oxidation of CH_4 using O_2 as the oxidant, as explained below. We note that the generation of NO_x must be carefully regulated to prevent the release of excess NO_x that is not consumed in CH_4 oxidation at hazardous concentrations. If such excess cannot be avoided, an additional catalytic conversion step should be implemented to ensure its safe removal.

Fierro *et al.* [53] reported that the addition of NO to O_2 increased CH_4 conversion on V_2O_5/SiO_2, which was attributed to gas-phase reactions promoted by NO as a radical initiator. It was shown in [54] that at lower temperatures (< 400 °C), the NO/NO_2 system forms an O atom shuttle, supplying O atoms to the catalyst surface. This NO-mediated O_2 dissociation allowed detectable CH_4 conversion on various transition metal oxide catalysts under conditions where negligible conversion occurs with O_2 alone. Similarly, [55] showed that the addition of NO alleviates the transient deactivation of Pd/Al_2O_3 through the formation of gas phase NO_2 that increased the content of more active PdO on the catalyst surface.

The enhanced catalyst reactivity in the presence of NO_x may allow for milder reactor conditions, enabling the conversion of CH_4 at lower temperatures. This has been demonstrated in literature, where enhanced CH_4 conversion over Pd-supported catalysts [56,57] was observed in the presence of NO_x. Similarly, the presence of NO_x enhanced the long-term activity and prevented the Pd-Pt/Al_2O_3 catalyst from deactivation in [58].

More importantly, the higher reactivity of NO_x could allow the use of less active catalysts that are more resistant against poisoning. This would offer a strong advantage over the conventional highly active catalysts, such as Pd-based catalysts, which are required for low-temperature combustion of CH_4 in air but are prone to severe deactivation due to poisoning. For instance, Ghampson *et al.* [54] demonstrated CH_4 conversion over various transition metal oxides at mild conditions of 300–400 °C in the presence of NO_x, whereas only using O_2 as oxidant showed much lower or no conversion.

Lastly, since thermal production of NO_x has been demonstrated to be quite efficient [25,59], the warm air plasma could function as an efficient heater to activate the catalytic conversion, powered by green electricity. Given the advantages discussed above, we believe that post-plasma CH_4 conversion through oxidation by NO_x species (produced by air plasma) at the catalyst surface is a promising new strategy worth exploring, potentially offering new catalyst candidates capable of operating under milder conditions and exhibiting greater resistance to poisoning.

Lastly, we note that our proposed strategy differs fundamentally from the simultaneous CH_4 abatement and NO_x formation for fertilizer production introduced in [1]. In case of the latter, the majority (if not all) of the barn air must be processed directly through the plasma reactor, and post-plasma injection must be minimized to avoid excessive dilution of NO_x. This is necessary to maintain a sufficiently high NO_x concentration (typically > 5 % [60,61]) for efficient downstream separation. Consequently, this configuration requires a very high energy input, resulting in high energy costs for CH_4 conversion, which must be justified by reaching a high enough NO_x yield.

In contrast, our proposed strategy treats only a small fraction of the barn air in the plasma reactor. The resulting plasma effluent is then significantly diluted with post-plasma barn air injection, since low NO_x

concentrations, e.g., 60 ppm [57], are already effective in promoting catalytic CH_4 oxidation by supplying O atoms to the catalyst surface. Moreover, the catalytic oxidation can proceed at relatively low temperatures (ca. 400 °C [27]), in stark contrast to the high temperatures (> 3000 K [59]) required for efficient thermal NO_x formation. As a result, the energy cost for CH_4 conversion in our approach can be substantially lower than that associated with the simultaneous CH_4 abatement and NO_x formation strategy.

8. Conclusions

We combined experiments and modeling to study the post-plasma removal of trace CH_4 concentrations in ambient air upon mixing the effluent of warm O_2 plasma with barn air. The model demonstrates satisfactory agreement with the experiments, so we can use it to explore the theoretical limits of the O_2 plasma effluent strategy, by systematically investigating a wide parameter space, including effluent temperatures, mixing rates, and flow rate ratios of plasma flow to barn air flow. The results indicate that the energy cost of CH_4 conversion (EC_{CH_4}) can be substantially reduced by increasing the mixing rate and flow rate ratio. Moreover, the high cooling rates resulting from these high mixing rates effectively supresses NO_x formation. The lowest energy cost of $EC_{CH_4} = 153$ MJ/mol is obtained at an effluent temperature of 3800 K, a characteristic mixing time of $\tau_{mix} = 0.1$ ms and a flow rate ratio of 30 (plasma flow to barn air flow), producing only 32 ppm NO_x. While this energy cost is lower than that of thermal conversion, i.e., ca. 220 MJ/mol, required to heat the barn air to ca. 1000 K where the 100 ppm CH_4 reacts away spontaneously, it is still higher than that of catalytic thermal oxidation (ca. 120 MJ/mol).

Our model reveals that the O atoms cannot be efficiently used to oxidize CH_4 owing to fast O atom recombination post-plasma. Therefore, the use of warm O_2 plasma effluent proves to be unviable for the removal of CH_4 traces within barn air. On the other hand, we propose that other plasma-generated reactive species with longer lifetimes than O atoms, such as ozone (O_3) and nitrogen oxides (NO_x), may offer more effective alternatives for CH_4 oxidation. In future work, the CANMILK project therefore aims to investigate the use of NO_x produced by warm air plasma to oxidize CH_4 at a catalyst surface. This approach can utilize the residual thermal energy to activate catalytic conversion, while leveraging the higher reactivity of NO_x relative to O_2 to potentially reduce the required operating temperature and enable the use of catalysts more resistant to poisoning than conventional Pd-based systems, thereby broadening the range of viable catalytic materials.

CRediT authorship contribution statement

Matthias Albrechts: Writing – original draft, Validation, Methodology, Investigation, Conceptualization. **Stijn Helsloot:** Writing – original draft, Validation, Methodology, Investigation, Data curation, Conceptualization. **Ivan Tsonev:** Writing – review & editing, Supervision, Methodology, Investigation, Conceptualization. **Niek den Harder:** Writing – review & editing, Supervision, Methodology, Investigation, Conceptualization. **Gerard van Rooij:** Supervision, Resources, Project administration, Funding acquisition, Conceptualization. **Annemie Bogaerts:** Writing – review & editing, Supervision, Resources, Project administration, Funding acquisition, Conceptualization.

Declaration of Competing Interest

None to declare.

Acknowledgements

This research was supported by the Horizon Europe Framework Program “Research and Innovation Actions” (RIA), project CANMILK (Grant No. 101069491), the FWO postdoc project of I. Tsonev (grant ID 1220326 N), and the European Research Council (ERC) under the European Union’s Horizon 2020 research and innovation programme (grant agreement No. 810182–SCOPE ERC Synergy project).

Appendix A. Supporting information

Supplementary data associated with this article can be found in the online version at doi:10.1016/j.jece.2025.120529.

Data availability

No data was used for the research described in the article.

References

[1] S. Helsloot, O. Samadi, M. Iqbal, G. van Rooij, T. Butterworth, Trace Methane Destruction within the Effluent of Microwave Plasma, ACS Omega (2025).
[2] A. Marmier, J. Schosger, Methane as greenhouse gas, EUR (2020).
[3] P. Forster, T. Storelvmo, K. Armour, W. Collins, J.-L. Dufresne, D. Frame, D. Lunt, T. Mauritsen, M. Palmer, M. Watanabe, Earth’S. Energy Budg. Clim. Feedbacks Clim. Sensit. (2021).
[4] S. Abernethy, M.I. Kessler, R.B. Jackson, Assessing the potential benefits of methane oxidation technologies using a concentration-based framework, Environ. Res. Lett. 18 (9) (2023) 094064.
[5] J. Yang, L. Yang, J. Zhang, X. Fan, S. Li, L. Zhang, W. Zhang, Experimental Study on Ultra-Low Concentration Methane Regenerative Thermal Oxidation, Energies 17 (9) (2024) 2109.
[6] L. He, Y. Fan, J. Bellettre, J. Yue, L. Luo, A review on catalytic methane combustion at low temperatures: Catalysts, mechanisms, reaction conditions and reactor designs, Renew. Sustain. Energy Rev. 119 (2020) 109589.
[7] M. Krogsbøll, H.S. Russell, M.S. Johnson, A high efficiency gas phase photoreactor for eradication of methane from low-concentration sources, Environ. Res. Lett. 19 (1) (2023) 014017.
[8] P. Gélin, M. Primet, Complete oxidation of methane at low temperature over noble metal based catalysts: a review, Appl. Catal. B Environ. 39 (1) (2002) 1–37.
[9] M. Monai, T. Montini, R.J. Gorte, P. Fornasiero, Catalytic oxidation of methane: Pd and beyond, Eur. J. Inorg. Chem. 2018 (25) (2018) 2884–2893.
[10] S. Yoon, J.N. Carey, J.D. Semrau, Feasibility of atmospheric methane removal using methanotrophic biotrickling filters, Appl. Microbiol. Biotechnol. 83 (2009) 949–956.
[11] X. Chen, Y. Li, X. Pan, D. Cortie, X. Huang, Z. Yi, Photocatalytic oxidation of methane over silver decorated zinc oxide nanocatalysts, Nat. Commun. 7 (1) (2016) 12273.
[12] K.A. Beauchemin, E.M. Ungerfeld, A.L. Abdalla, C. Alvarez, C. Arndt, P. Becquet, C. Benchaar, A. Berndt, R.M. Mauricio, T.A. McAllister, Invited review: Current enteric methane mitigation options, J. Dairy Sci. 105 (12) (2022) 9297–9326.
[13] R.B. Jackson, S. Abernethy, J.G. Canadell, M. Cargnello, S.J. Davis, S. Féron, S. Fuss, A.J. Heyer, C. Hong, C.D. Jones, Atmospheric methane removal: a research agenda, Philos. Trans. R. Soc. A 379 (2210) (2021) 20200454.
[14] M.S. Johnson, E.J. Nilsson, E.A. Svensson, S. Langer, Gas-phase advanced oxidation for effective, efficient in situ control of pollution, Environ. Sci. Technol. 48 (15) (2014) 8768–8776.
[15] G. Grossi, P. Goglio, A. Vitali, A.G. Williams, Livestock and climate change: impact of livestock on climate and mitigation strategies, Anim. Front. 9 (1) (2019) 69–76.
[16] T. Nozaki, K. Okazaki, Non-thermal plasma catalysis of methane: Principles, energy efficiency, and applications, Catal. Today 211 (2013) 29–38.
[17] U. Kogelschatz, Dielectric-barrier discharges: their history, discharge physics, and industrial applications, Plasma Chem. Plasma Process. 23 (1) (2003) 1–46.
[18] M. Kaiser, K.M. Baumgärtner, A. Mattheus, Microwave plasma sources-applications in industry, Contrib. Plasma Phys. 52 (7) (2012) 629–635.
[19] G. Franz, Low pressure plasmas and microstructuring technology, Springer Science & Business Media, 2009.
[20] F. Rodrigues, J. Pascoa, M. Trancossi, Heat generation mechanisms of DBD plasma actuators, Exp. Therm. Fluid Sci. 90 (2018) 55–65.
[21] A.K. Singh, J. Palo, J. Kihlman, T. Heikola, M. Suvanto, P. Simell, N.M. Kinnunen, Non-thermal plasma assisted methane oxidation inside a DBD reactor: Effect of monometallic catalyst on energy efficiency and CO2 selectivity, Chem. Eng. J. 521 (2025) 166610.
[22] M.F. Mustafa, X. Fu, W. Lu, Y. Liu, Y. Abbas, H. Wang, M.T. Arslan, Application of non-thermal plasma technology on fugitive methane destruction: Configuration and optimization of double dielectric barrier discharge reactor, J. Clean. Prod. 174 (2018) 670–677.
[23] M. Albrechts, I. Tsonev, A. Bogaerts, Investigation of O atom kinetics in O2 plasma and its afterglow, Plasma Sources Sci. Technol. 33 (4) (2024) 045017.
[24] R. Snoeckx, A. Bogaerts, Plasma technology–a novel solution for CO 2 conversion? Chem. Soc. Rev. 46 (19) (2017) 5805–5863.
[25] S. Kelly, A. Bogaerts, Nitrogen fixation in an electrode-free microwave plasma, Joule 5 (11) (2021) 3006–3030.
[26] Z. Li, G.B. Hoflund, A review on complete oxidation of methane at low temperatures, J. Nat. Gas. Chem. 12 (3) (2003) 153–160.

[27] R. Burch, F. Urbano, P. Loader, Methane combustion over palladium catalysts: The effect of carbon dioxide and water on activity, Appl. Catal. A Gen. 123 (1) (1995) 173–184.
[28] A. Setiawan, J. Friggieri, E.M. Kennedy, B.Z. Dlugogorski, M. Stockenhuber, Catalytic combustion of ventilation air methane (VAM)–long term catalyst stability in the presence of water vapour and mine dust, Catal. Sci. Technol. 4 (6) (2014) 1793–1802.
[29] D. Colombari, F. Masoero, A. Della Torre, A CFD Methodology for the Modelling of Animal Thermal Welfare in Hybrid Ventilated Livestock Buildings, AgriEngineering 6 (2) (2024) 1525–1548.
[30] X. Yang, X. Long, X. Yao, Numerical investigation on the mixing process in a steam ejector with different nozzle structures, Int. J. Therm. Sci. 56 (2012) 95–106.
[31] S. Helsloot, "GUI_FTIR,", 2025. [Online]. Available: ⟨https://github.com/StijnHelsl98t/GUI_FTIR⟩.
[32] M. Ruijzendaal, "Brightsite-Plasmalab/ramlab," Maastricht University, 2025. [Online]. Available: ⟨https://github.com/Brightsite-Plasmalab/ramlab⟩. [Accessed 2025].
[33] G. Herzberg, Infrared and Raman spectra of polyatomic molecules, 2, van Nostrand, 1945.
[34] R. Clark, D. Long, Raman spectroscopy, McGraw-Hill, New York, 1977.
[35] M.A. Buldakov, V.N. Cherepanov, B.V. Korolev, I.I. Matrosov, Role of intramolecular interactions in Raman spectra of N2 and O2 molecules, J. Mol. Spectrosc. 217 (1) (2003) 1–8.
[36] A.W. van de Steeg, L. Vialetto, A. Silva, F. Peeters, D.C. van den Bekerom, N. Gatti, P. Diomede, M. Van de Sanden, G.J. van Rooij, Revisiting spontaneous Raman scattering for direct oxygen atom quantification, Opt. Lett. 46 (9) (2021) 2172–2175.
[37] D. Del Cont-Bernard, M. Ruijzendaal, T. Righart, G. van Rooij, T. Butterworth, 2D Raman imaging for vibrational and rotational temperature mapping in H2, J. Quant. Spectrosc. Radiat. Transf. 328 (2024) 109145.
[38] *COMSOL Multiphysics® v. 6.0.* ⟨www.comsol.com⟩. *COMSOL AB, Stockholm, Sweden.*
[39] M. Albrechts, I. Tsonev, A. Bogaerts, Can post-plasma CH 4 injection improve plasma-based dry reforming of methane? A modeling study, Green. Chem. 26 (18) (2024) 9712–9728.
[40] Gregory P. Smith, D.M.G., Michael Frenklach, Nigel W. Moriarty, Boris Eiteneer, Mikhail Goldenberg, C.Thomas Bowman, Ronald K. Hanson, Soonho Song, William C.. Gardiner, Jr., Vitali V. Lissianski, and Zhiwei Qin GRI-Mech 3.0. ⟨http://www.me.berkeley.edu/gri_mech/⟩.
[41] F. D'Isa, E. Carbone, A. Hecimovic, U. Fantz, Performance analysis of a 2.45 GHz microwave plasma torch for CO2 decomposition in gas swirl configuration, Plasma Sources Sci. Technol. 29 (10) (2020) 105009.
[42] M. Tatar, V. Vashisth, M. Iqbal, T. Butterworth, G. van Rooij, R. Andersson, Analysis of a plasma reactor performance for direct nitrogen fixation by use of three-dimensional simulations and experiments, Chem. Eng. J. 497 (2024) 154756.
[43] Y. Kabouzi, M. Calzada, M. Moisan, K. Tran, C. Trassy, Radial contraction of microwave-sustained plasma columns at atmospheric pressure, J. Appl. Phys. 91 (3) (2002) 1008–1019.
[44] J. Wang, X. Huang, G. Gong, M. Hao, F. Yin, A systematic study of the residual gas effect on vacuum solar receiver, Energy Convers. Manag. 52 (6) (2011) 2367–2372.
[45] J.H. Ferziger, M. Perić, R.L. Street, Computational methods for fluid dynamics, springer, 2019.
[46] David G. Goodwin, Harry K. Moffat, Ingmar Schoegl, Raymond L. Speth, and Bryan W. Weber. Cantera: An object-oriented software toolkit for chemical kinetics, thermodynamics, and transport processes. ⟨https://www.cantera.org⟩, 2023. Version 3.0.0. doi:10.5281/zenodo.8137090.
[47] M.I. Boulos, P. Fauchais, E. Pfender, Thermal plasmas: fundamentals and applications, Springer Science & Business Media, 2013.
[48] Ishii, Y.; Ogawa, T.; Onda, K.; Miyagishi, H.; Ashikari, Y.; Nagaki, A.; Asano, S.; Miyata, K., Sub-Millisecond Mixing in a T-Mixer in the Turbulent Flow Regime: Quantitative Chemiluminescence-Based Analysis. 2025.
[49] N.-T. Nguyen, Micromixers: fundamentals, design and fabrication, William Andrew, 2011.
[50] A. a Alizadeh, D.J. Jasim, N. Sohrabi, M. Ahmed, S.A. Ameer, S.M. Ibrahim, H. K. Dabis, A.A. Hussein, A.J. Sultan, Using shock generator for the fuel mixing of the extruded single 4-lobe nozzle at supersonic combustion chamber, Sci. Rep. 14 (1) (2024) 6405.
[51] J.P. Drummond, G.S. Diskin, A. Cutler, Chapter 6: fuel–air mixing and combustion in scramjets. *Technologies for Propelled Hypersonic Flight, NATO-RTO-AVT*, Natl. Tech. Inf. Serv. Va. USA 13 (2006) 17.
[52] Y. Li, J. Jiang, M. Hinshelwood, S. Zhang, P.J. Bruggeman, G.S. Oehrlein, Characterization of plasma catalytic decomposition of methane: role of atomic O and reaction mechanism, J. Phys. D Appl. Phys. 55 (15) (2022) 155204.
[53] M.A. Bañares, J.H. Cardoso, G.J. Hutchings, J.M. Correa Bueno, J.L. Fierro, Selective oxidation of methane to methanol and formaldehyde over V2O5/SiO2 catalysts. Role of NO in the gas phase, Catal. Lett. 56 (2) (1998) 149–153.
[54] I.T. Ghampson, S.-T.B. Lundin, V. Vargheese, Y. Kobayashi, G.S. Huff, R. Schlögl, A. Trunschke, S.T. Oyama, Methane selective oxidation on metal oxide catalysts at low temperatures with O2 using an NO/NO2 oxygen atom shuttle, J. Catal. 408 (2022) 401–412.
[55] C. Cui, Y. Zhang, W. Shan, Y. Yu, H. He, Influence of NOx on the activity of Pd/θ-Al2O3 catalyst for methane oxidation: Alleviation of transient deactivation, J. Environ. Sci. 112 (2022) 38–47.
[56] M. Öcal, R. Oukaci, G. Marcelin, B.W. Jang, J.J. Spivey, Steady-state isotopic transient kinetic analysis on Pd-supported hexaaluminates used for methane combustion in the presence and absence of NO, Catal. Today 59 (1-2) (2000) 205–217.
[57] P. Hurtado, S. Ordóñez, H. Sastre, F.V. Díez, Combustion of methane over palladium catalyst in the presence of inorganic compounds: inhibition and deactivation phenomena, Appl. Catal. B Environ. 47 (2) (2004) 85–93.
[58] A.T. Gremminger, H.W.P. de Carvalho, R. Popescu, J.-D. Grunwaldt, O. Deutschmann, Influence of gas composition on activity and durability of bimetallic Pd-Pt/Al2O3 catalysts for total oxidation of methane, Catal. Today 258 (2015) 470–480.
[59] I. Tsonev, C. O'Modhrain, A. Bogaerts, Y. Gorbanev, Nitrogen fixation by an arc plasma at elevated pressure to increase the energy efficiency and production rate of no x, ACS Sustain. Chem. Eng. 11 (5) (2023) 1888–1897.
[60] K.H.R. Rouwenhorst, S. Tabak, L. Lefferts, Improving the energy yield of plasma-based NO x synthesis with in situ adsorption, React. Chem. Eng. 9 (3) (2024) 528–531.
[61] W. Dekker, E. Snoeck, H. Kramers, The rate of absorption of NO2 in water, Chem. Eng. Sci. 11 (1) (1959) 61–71.